Decisive role of electron-phonon coupling for phonon and electron instabilities in transition metal dichalcogenides

Zishen Wang [1,2,*] Chuan Chen [3,4,*] Jinchao Mo [1] Jun Zhou [5,†] Kian Ping Loh [2,6,‡] and Yuan Ping Feng [1,2,§]

[1]Department of Physics, National University of Singapore, Singapore 117542, Singapore

[2]Centre for Advanced 2D Materials, National University of Singapore, Singapore 117546, Singapore

[3]Institute for Advanced Study, Tsinghua University, Beijing 100084, China

[4]Max-Planck Institute for the Physics of Complex Systems, 01187 Dresden, Germany

[5]Institute of Materials Research & Engineering, A*STAR (Agency for Science, Technology and Research), Singapore 138634, Singapore

[6]Department of Chemistry, National University of Singapore, Singapore 117543, Singapore

The origin of the charge density wave (CDW) in transition metal dichalcogenides has been hotly debated, and no conclusive agreement has been reached. Here, we propose an *ab initio* framework for an accurate description of both Fermi surface nesting and electron-phonon coupling (EPC) and systematically investigate their roles in the formation of the CDW. Using monolayer $1H$-NbSe$_2$ and $1T$-VTe$_2$ as representative examples, we show that it is the momentum-dependent EPC that softens the phonon frequencies, which become imaginary (phonon instabilities) at CDW vectors (indicating CDW formation). In addition, the distribution of the CDW gap opening (electron instabilities) can be correctly predicted only if EPC is included in the mean-field model. These results emphasize the decisive role of EPC in the CDW formation. Our analytical process is general and can be applied to other CDW systems.

I. INTRODUCTION

The formation of a charge density wave (CDW) is a spontaneous symmetry breaking process with periodic charge density modulations and lattice distortions below a critical temperature T_{CDW} [1,2]. However, the origin of CDWs is a long-standing problem, which has attracted broad research interest [3–6]. The first mechanism, Fermi surface nesting (FSN), relates to elastic electronic scatterings at the Fermi surface [7]. The zero-energy electronic excitations screen the phonon vibration at the CDW vector, inducing an abrupt phonon softening [8].

In contrast, momentum-dependent electron-phonon coupling (**q**-EPC) involves inelastic electronic scatterings mediated by phonons, in which the electron field can be integrated out as a perturbation to the free phonon field, softening phonon frequencies from their bare values. Thus, both FSN and **q**-EPC may soften phonons to imaginary values (phonon instabilities) and induce CDW distortions. However, quantitative studies of **q**-EPC are rare, and the only report is a

tight-binding (TB) model merely using the electronic band structure [9–12]. However, this semiempirical method has difficulty giving rigorous results compared to the first-principles calculations. Therefore, a general method to accurately describe **q**-EPC is urgently needed.

In addition, the CDW gap opening (electron instabilities) is less studied. The location of the CDW gap in the Brillouin zone (BZ) can be identified by band unfolding [13–15], which, however, requires prior knowledge of the CDW structure and cannot reveal the underlying mechanism. Thus, the driving force of the CDW gap is still elusive.

In this work, we use monolayer $1H$-NbSe$_2$ and $1T$-VTe$_2$ (abbreviated to NbSe$_2$ and VTe$_2$) as representative examples of the most common high-symmetry phases of the transition metal dichalcogenides (TMDs). Interestingly, the mechanisms of their CDWs are considered to be different. The electron-phonon coupling (EPC) has been shown to be dominant in NbSe$_2$ [14,16,17], while FSN in VTe$_2$ seems to be substantial, which leads to a peak in the static Lindhard susceptibility [18,19]. Thus, we conduct a comprehensive study of their CDW properties from both phononic and electronic perspectives. The accurate **q**-EPC from the fully first-principles calculations allows us to make a straightforward comparison between the contributions from FSN and **q**-EPC in the CDW formation. Interestingly, the **q**-EPC is shown to play a dominant role in designating the CDW vectors for both NbSe$_2$ and VTe$_2$. We also find the rigorous EPC matrix elements are the key to predict the **k**-space distribution of the CDW gaps by our mean-field model. More importantly, our analysis process, besides being concise and accurate, is a general framework which can easily be exploited in other CDW systems.

---

*These authors contributed equally to this work.

†zhou_jun@imre.a-star.edu.sg

‡chmlohkp@nus.edu.sg

§phyfyp@nus.edu.sg
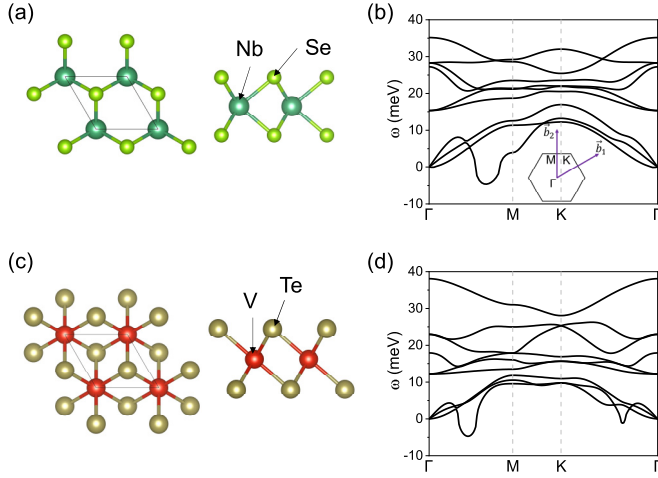
FIG. 1. (a) Top and side views of the crystal structure and (b) phonon dispersion of monolayer $1H$-NbSe$_2$. (c) and (d) Same as (a) and (b), but for monolayer $1T$-VTe$_2$. The inset in (b) displays the first BZ with reciprocal lattice vectors.

II. COMPUTATIONAL METHOD

The calculations were obtained using the QUANTUM ESPRESSO package [20,21]. Norm-conserving pseudopotentials [22] with an energy cutoff of 80 Ry were used in the calculations. A vacuum of 15 Å was used between periodic layers. All the structures were fully relaxed until the force and energy were less than 4×10^{-6} Ry/bohr and 10^{-10} Ry. We used $16 \times 16 \times 1$ and $8 \times 8 \times 1$ meshes to sample the electronic and phononic BZs, respectively. The EPC properties were calculated with the EPW code [23] with dense $64 \times 64 \times 1$ **k** and **q** grids. To avoid an ill definition of the EPC of imaginary phonons, the EPC matrix elements are calculated by a slightly large smearing, where the phonon branch shows a Kohn anomaly [16]. The susceptibility was calculated with a $111 \times 111 \times 1$ electron-momentum grid at 145 K for NbSe$_2$ [24,25] and 186 K for VTe$_2$ [18]. All electronic states of the band which crosses the Fermi level are involved in the susceptibility calculations.

III. RESULTS

A. Phonon instabilities and CDW mechanism

In TMDs, transition metal atoms are sandwiched by chalcogen atoms, forming trigonal prisms (a $1H$ phase) or octahedrons (a $1T$ phase). The structures of $1H$-NbSe$_2$ and $1T$-VTe$_2$ are shown in Figs. 1(a) and 1(c), respectively. As the phonon spectra for NbSe$_2$ and VTe$_2$ show in Figs. 1(b) and 1(d), their longitudinal acoustic (LA) phonon modes collapse at the CDW vectors, which triple the unit cell for NbSe$_2$ with $\mathbf{Q}^{\mathbf{H}} = 2/3\Gamma M$ and quadruple the unit cell for VTe$_2$ with $\mathbf{Q}^{\mathbf{T}} = 1/2\Gamma M$, in line with the CDW supercells in experiments [18,26–28].

The relationship between the softened phonon frequency $\omega_{\mathbf{q}}$ and its bare phonon frequency $\Omega_{\mathbf{q}}$ can be described under the random phase approximation (more details are given in Appendix B):

$$\omega_{\mathbf{q}}^2 = \Omega_{\mathbf{q}}^2 - 2\Omega_{\mathbf{q}}\chi_{\mathbf{q}}, \qquad (1)$$

where $\chi_{\mathbf{q}}$ is the generalized static electronic susceptibility, including contributions from both FSN and EPC, which is given by

$$\chi_{\mathbf{q}} = \sum_{\mathbf{k}} |g_{\mathbf{k},\mathbf{k}+\mathbf{q}}|^2 \frac{f(\varepsilon_{\mathbf{k}}) - f(\varepsilon_{\mathbf{k}+\mathbf{q}})}{\varepsilon_{\mathbf{k}+\mathbf{q}} - \varepsilon_{\mathbf{k}}}, \qquad (2)$$

where $f(\varepsilon)$ is the Fermi-Dirac function of the eigenvalue ε and $g_{\mathbf{k},\mathbf{k}+\mathbf{q}}$ is the EPC matrix element that couples electronic states **k** and **k+q** with a phonon of momentum **q**. According to Eq. (1), the ordering vector is estimated from the maximum of $\chi_{\mathbf{q}}$ [10,11]. $\chi_{\mathbf{q}}$ often reduces to the static Lindhard susceptibility $\chi'_{\mathbf{q}}$ under the constant matrix element approximation ($|g_{\mathbf{k},\mathbf{k}+\mathbf{q}}| = 1$):

$$\chi'_{\mathbf{q}} = \sum_{\mathbf{k}} \frac{f(\varepsilon_{\mathbf{k}}) - f(\varepsilon_{\mathbf{k}+\mathbf{q}})}{\varepsilon_{\mathbf{k}+\mathbf{q}} - \varepsilon_{\mathbf{k}}}, \qquad (3)$$

which is a pure electron effect, and its peak reflects the electronic instability by FSN [4]. Similarly, $\chi_{\mathbf{q}}$ can reduce to the **q**-EPC $\bar{g}_{\mathbf{q}}$ under the "constant fraction" approximation ($\frac{f(\varepsilon_{\mathbf{k}}) - f(\varepsilon_{\mathbf{k}+\mathbf{q}})}{\varepsilon_{\mathbf{k}+\mathbf{q}} - \varepsilon_{\mathbf{k}}} = 1$):

$$\bar{g}_{\mathbf{q}} = \sum_{\mathbf{k}} |g_{\mathbf{k},\mathbf{k}+\mathbf{q}}|^2, \qquad (4)$$

which reflects a pure EPC effect. Only the low-energy interaction around the Fermi level is considered by the coupling between the lowest phonon branch and the single electronic band which crosses the Fermi level [the pink bands in Figs. 5(b) and 5(e)]. Due to the complexity in describing the EPC matrix elements, only static Lindhard susceptibility has been widely used, while the **q**-EPC, which may play a more important role, is ignored [4,6].

To remedy this blemish, we applied density functional perturbation theory (DFPT) to obtain the accurate element g [29] by

$$g_{\mathbf{k},\mathbf{k}+\mathbf{q}} = \left(\frac{\hbar}{2M\omega_{\mathbf{q}}}\right)^{1/2} \langle \varphi_{\mathbf{k}+\mathbf{q}} | \partial_{\mathbf{q}} V | \varphi_{\mathbf{k}} \rangle, \qquad (5)$$

where $\partial_{\mathbf{q}} V$ is the derivative of the electron-ion potential and $\varphi_{\mathbf{k}}$ is the electronic wave function with wave vector **k**. For a direct comparison, we also calculated the matrix element g between electronic states **k** and **k+q** with the previously used TB model [9–12]:

$$g_{\mathbf{k},\mathbf{k}+\mathbf{q}} \propto (\nu_{\mathbf{k}} - \nu_{\mathbf{k}+\mathbf{q}}) \cdot \frac{\mathbf{q}}{|\mathbf{q}|}, \qquad (6)$$

where $\nu_{\mathbf{k}}$ is the electron velocity at the **k** point in the coupled band and $\frac{\mathbf{q}}{|\mathbf{q}|}$ is the longitudinal projection as only LA phonons soften to zero. The quantities obtained with the TB method are denoted as $\bar{g}_{\mathbf{q}}^{\text{TB}}$ and $\chi_{\mathbf{q}}^{\text{TB}}$, while the ones from DFPT are $\bar{g}_{\mathbf{q}}$ and $\chi_{\mathbf{q}}$.

The calculated $\chi'_{\mathbf{q}}$, $\bar{g}_{\mathbf{q}}$, $\chi_{\mathbf{q}}$, and $\omega_{\mathbf{q}}$ for NbSe$_2$ (top panels) and VTe$_2$ (bottom panels) are shown in Fig. 2. For NbSe$_2$, the static Lindhard susceptibility $\chi'_{\mathbf{q}}$ has a broad plateau from $2/5\Gamma M$ to $4/5\Gamma M$ [Fig. 2(a) and the blue line in Fig. 3(a)], suggesting the weakness of FSN [17]. Nonetheless, $\bar{g}_{\mathbf{q}}$ exhibits a strong EPC near $2/3\Gamma M$ for NbSe$_2$ [Fig. 2(b) and the red line in Fig. 3(a)]. In addition, the topology of $\chi_{\mathbf{q}}$ is very similar to $\bar{g}_{\mathbf{q}}$ [Figs. 2(b) and 2(c)], indicating the dominant role
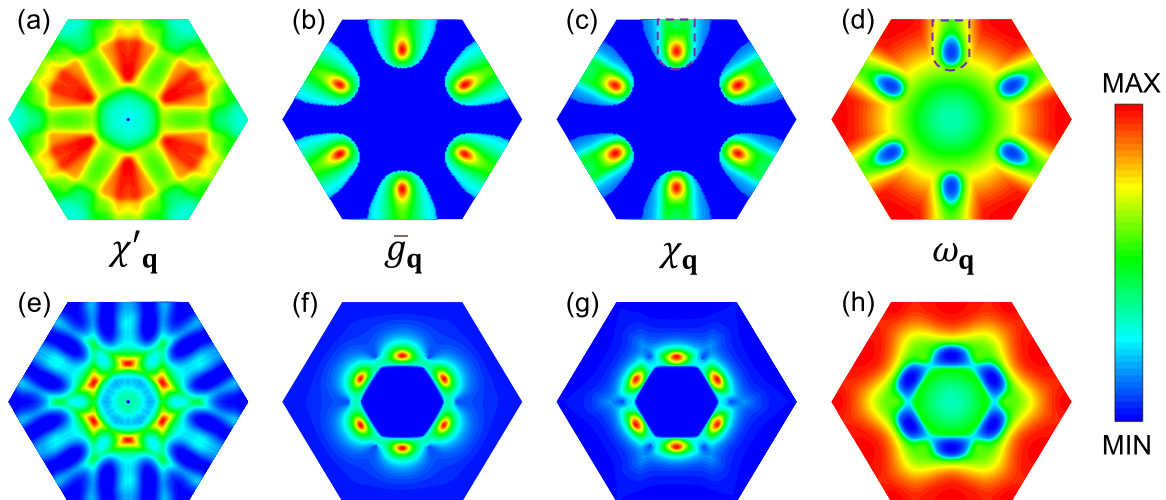
FIG. 2. (a) Static Lindhard susceptibility $\chi'_{\mathbf{q}}$, (b) **q**-EPC $\bar{g}_{\mathbf{q}}$, (c) generalized static electronic susceptibility $\chi_{\mathbf{q}}$, and (d) the lowest phonon branch frequency $\omega_{\mathbf{q}}$ in the first BZ of NbSe$_2$. (e)–(h) Same as (a)–(d), but for VTe$_2$.

played by the **q**-EPC in $\chi_{\mathbf{q}}$. Figure 2(d) displays the softened phonons of NbSe$_2$, which are concentrated in the archlike area [the purple dashed line in Fig. 2(d)], in agreement with the highland in $\chi_{\mathbf{q}}$ [the purple dashed line in Fig. 2(c)]. More importantly, the peaks in $\bar{g}_{\mathbf{q}}$ and $\chi_{\mathbf{q}}$ [the red areas in Figs. 2(b) and 2(c)] are at $2/3\Gamma M$, consistent with the dip in $\omega_{\mathbf{q}}$ [the blue areas in Fig. 2(d)].

The EPC properties of bulk $2H$-NbSe$_2$ were well described by the TB method [10,11]; however, we find this method fails for monolayer $1H$-NbSe$_2$. As for the generalized static electronic susceptibility $\chi_{\mathbf{q}}^{\text{TB}}$, the overall topology in the first BZ [Fig. 7(c)] cannot fit the phonon softening [Fig. 2(d)], in stark contrast to the good match achieved by DFPT [Fig. 2(c)].

Furthermore, the peaks of $\bar{g}_{\mathbf{q}}^{\text{TB}}$ and $\chi_{\mathbf{q}}^{\text{TB}}$ in the ΓM path [the green line in Fig. 3(a) and the orange line in Fig. 3(b)] are near $1/2\Gamma M$, which predicts the formation of a 4×4 instead of a 3×3 CDW. By making a comparison to the prominent peaks of $\bar{g}_{\mathbf{q}}$ and $\chi_{\mathbf{q}}$ at $2/3\Gamma M$ obtained with the DFPT [the red line in Fig. 3(a) and the black line in Fig. 3(b)], we conclude the *ab initio* based DFPT method is superior to the TB method for obtaining the **q**-EPC and predicting the CDW vector in monolayer NbSe$_2$.

For monolayer VTe$_2$, $\chi'_{\mathbf{q}}$ has a peak near $2/5\Gamma M$ [Fig. 2(e) and the blue line in Fig. 3(c)], in line with previous works [18,19]. However, this peak does not correspond to the 4×4 CDW from experiments [18,28]. In addition, the profile of $\chi_{\mathbf{q}}$ is close to $\bar{g}_{\mathbf{q}}$ [Figs. 2(f) and 2(g)], which both show maxima close to $1/2\Gamma M$, providing a powerful clue about phonon softening at $\mathbf{Q}^{\mathbf{T}}$. As shown in Fig. 2(h), the distribution of the softened phonon frequency $\omega_{\mathbf{q}}$ of VTe$_2$ shows a hexapetalous flowerlike pattern [the blue area in Fig. 2(h)], which matches the "hot" area in $\chi_{\mathbf{q}}$ well [Fig. 2(g)]. Furthermore, the sharp peak of $\bar{g}_{\mathbf{q}}$ overwhelms the fluctuation of $\chi'_{\mathbf{q}}$ in VTe$_2$ [the red and blue lines in Fig. 3(c)], leading to the correct $1/2\Gamma M$ peak position of $\chi_{\mathbf{q}}$ [the black line in Fig. 3(d)]. Again, the TB method cannot explain the phonon softening in VTe$_2$. Although $\bar{g}_{\mathbf{q}}^{\text{TB}}$ shows a peak at $1/2\Gamma M$, this peak is even broader than the nesting peak at $2/5\Gamma M$, leading to the incorrect peak position of $\chi_{\mathbf{q}}^{\text{TB}}$ at $2/5\Gamma M$ [the green line in Fig. 3(c) and the orange line in Fig. 3(d)]. Compared to the distribution of $\bar{g}_{\mathbf{q}}^{\text{TB}}$ [Fig. 7(e)], the "sharpness" of $\chi'_{\mathbf{q}}$ makes the topology of $\chi_{\mathbf{q}}^{\text{TB}}$ closer to that of $\chi'_{\mathbf{q}}$ in the first BZ of VTe$_2$ [Figs. 2(e) and 7(f)], which cannot explain the phonon softening shown in Fig. 2(h). Therefore, with the help of the accurate EPC matrix element g obtained with DFPT, our study clearly demonstrates that **q**-EPC rather than FSN determines the phonon softening and accounts for the CDW formation in both NbSe$_2$ and VTe$_2$.
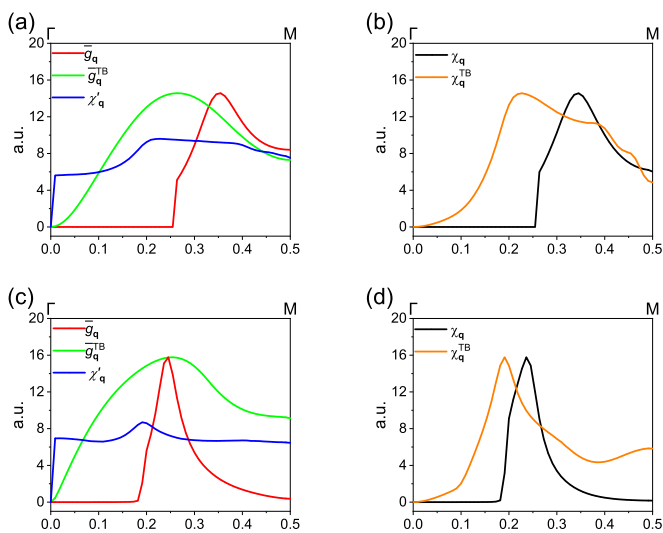
FIG. 3. Direct comparison of the role of EPC and FSN along the ΓM path in NbSe$_2$ (top) and VTe$_2$ (bottom). (a) Comparison of the differences among $\bar{g}_{\mathbf{q}}$ (red), $\bar{g}_{\mathbf{q}}^{\text{TB}}$ (green), and $\chi'_{\mathbf{q}}$ (blue) in NbSe$_2$. (b) Comparison of the difference between $\chi_{\mathbf{q}}$ (black) and $\chi_{\mathbf{q}}^{\text{TB}}$ (orange) in NbSe$_2$. (c) and (d) Same as (a) and (b), but for VTe$_2$. Note that the unit of the y coordinate is arbitrary units (a.u.) for straightforward comparison.

B. Electron instabilities and CDW gaps

The Hamiltonian of the CDW phase is minimally described by including one band crossing the Fermi level and
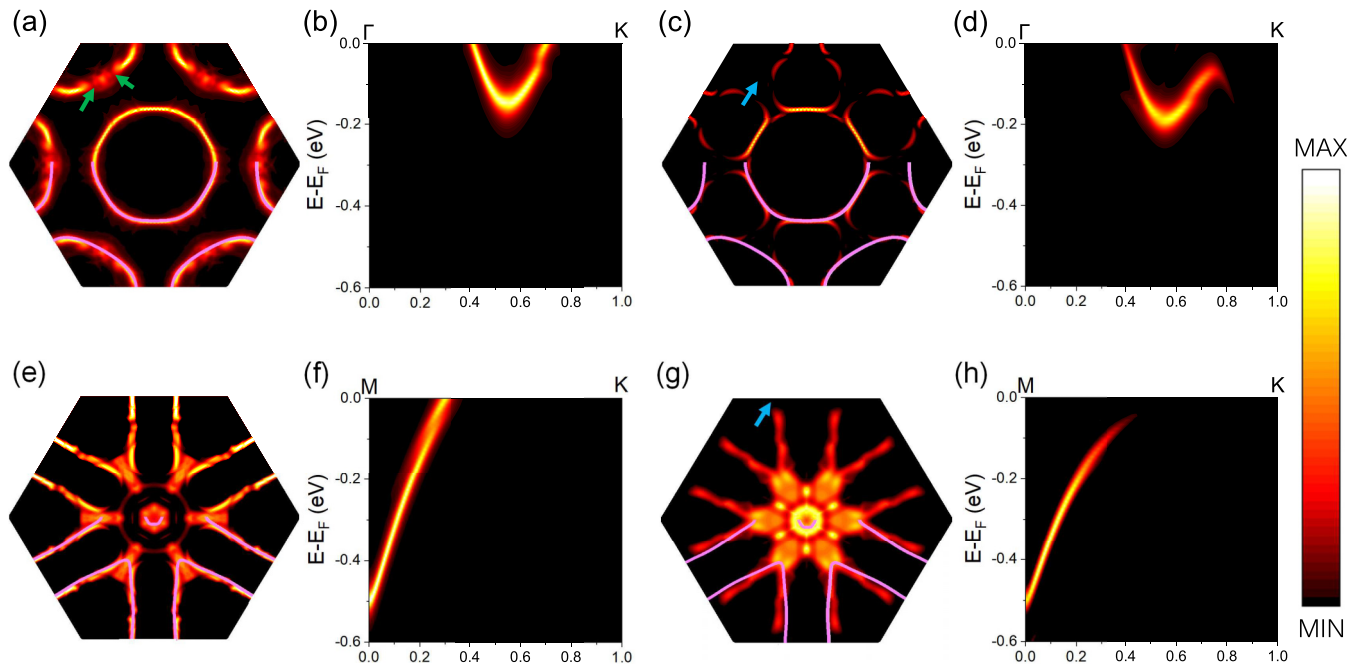
FIG. 4. (a) Fermi surface and (b) spectral function along ΓK with constant $|g|$ for the NbSe$_2$ CDW system. (c) and (d) Same as (a) and (b), but with anisotropic g. (e) Fermi surface and (f) spectral function along MK with constant $|g|$ for the VTe$_2$ CDW system. (g) and (h) Same as (e) and (f), but with anisotropic g in the simulation. The brightness of the dots denotes the spectral weights. The pink solid lines in (a), (c), (e), and (g) in the lower half of the BZ are the corresponding non-CDW Fermi surfaces for comparison. The green arrows in (a) indicate the partial CDW gaps opened by FSN, while the blue arrows in (c) and (g) indicate the full CDW gaps opened by FSN + EPC. The paths of the spectral functions are chosen to better show the full CDW gaps.

electron-phonon interaction with phonon momentum **Q**:

$$H_{mf} = \sum_{\mathbf{k}} \varepsilon_{\mathbf{k}} c_{\mathbf{k}}^{\dagger} c_{\mathbf{k}} + \sum_{\mathbf{k},\mathbf{Q}} 2g_{\mathbf{k},\mathbf{k}+\mathbf{Q}} \Delta_{\mathbf{Q}} c_{\mathbf{k}}^{\dagger} c_{\mathbf{k}+\mathbf{Q}} + \text{H.c.} \quad (7)$$

Here, $c_{\mathbf{k}}^{\dagger}$ ($c_{\mathbf{k}}$) and $\varepsilon_{\mathbf{k}}$ are the creation (annihilation) operator and energy for an electron with momentum **k**. $\Delta_{\mathbf{Q}}$ is the order parameter, which was approximated to a constant because of symmetry and small pocket size. This Hamiltonian can then be used to calculate the spectral function of the CDW phases (see Appendix C for more details).

The simulated Fermi surface of the NbSe$_2$ CDW structure with constant EPC matrix elements $|g|$ (i.e., $|g| = \sum_{\mathbf{k},\mathbf{k}+\mathbf{Q}} |g_{\mathbf{k},\mathbf{k}+\mathbf{Q}}|/N_{\mathbf{k},\mathbf{k}+\mathbf{Q}}$, where $N_{\mathbf{k},\mathbf{k}+\mathbf{Q}}$ is the number of g in the calculation) reflects purely the FSN effect under the mean-field picture. The norm of g is used to avoid the arbitrary phase factor problem in the band basis of the EPC matrix element. As the green arrows show in Fig. 4(a), each K pocket has three couples of partial gaps, where the spectral intensity becomes blurred as only partial electronic states are left at the Fermi surface. The partial gaps are on both sides of the ΓK path, corresponding to the most heavily nested points of NbSe$_2$ [red points in white circles in Fig. 10(c)]. The incorporation of anisotropic matrix elements leads to a more extensive gap opening on the Fermi surface [Fig. 4(c)]. Remarkably, the full band gap sectors can be found in the K pockets, where the electronic states on the Fermi surface are completely obliterated [blue arrow in Fig. 4(c)]. Furthermore, the spectral function is plotted along the ΓK path. The pure nesting effect cannot open a band gap along this path

[Fig. 4(b)]. In contrast, the spectral function derived with the anisotropic g clearly exhibits a full band gap close to the K point [Fig. 4(d)]. Considering there is no experimental report of the Fermi surface of the monolayer NbSe$_2$ CDW state, the predicted CDW gap distribution is compared with the unfolded Fermi surface of the simulated NbSe$_2$ CDW ground state, and they display remarkable agreement (Fig. 2(b) in Ref. [16]).

The parallel sides of the triangular hole pockets for VTe$_2$ provide good nesting conditions [18,19]. Such nesting will induce a peak in the static Lindhard susceptibility and possibly open a CDW gap [18]. However, a constant-$|g|$ approximation [Fig. 4(e)] suggests that there is no obvious spectral weight depletion on the Fermi surface, and no CDW gap can be opened on the MK path [Figs. 4(e) and 4(f)]. Importantly, the inclusion of anisotropic g suppresses the spectral intensity near the M point [blue arrow in Fig. 4(g)]. No electronic state can be found on the Fermi surface in the MK path, indicating a full gap opening [Fig. 4(h)], consistent with the experimental results [18]. Moving toward the Γ point, the decreasing of the gap size is accompanied by the full to partial gap transition, and finally, the gap closes at the triangular K pocket apex [Fig. 4(g)]. Such an anisotropic gap distribution on the Fermi surface agrees well with the angle-resolved photoemission spectroscopy measurements (Fig. 3(a) in Ref. [18]).

IV. DISCUSSION

The underlying mechanism for CDW formation is still under debate after decades of intense study. Using NbSe$_2$
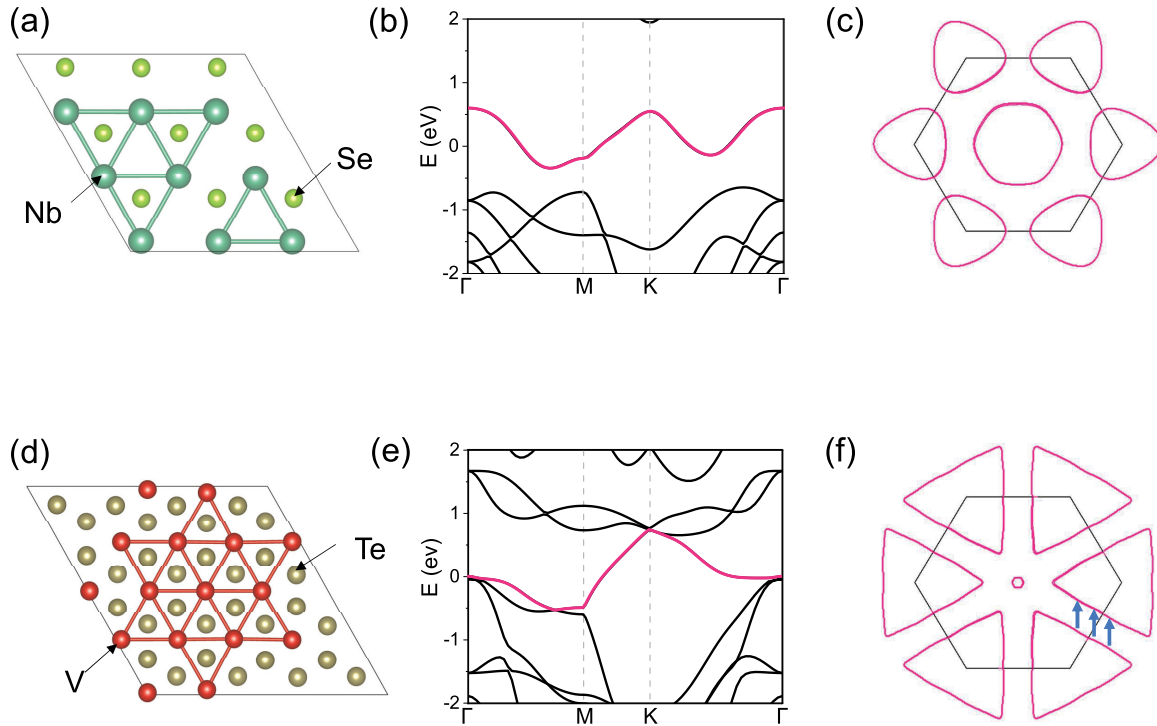
FIG. 5. (a) The 3×3 CDW structure of monolayer $1H$-NbSe$_2$. (b) Band structure and (c) Fermi surface of monolayer NbSe$_2$. (d) The 4×4 CDW structure of monolayer $1T$-VTe$_2$. (e) and (f) Same as (b) and (c), but for monolayer VTe$_2$. The electronic bands which cross the Fermi level are highlighted in pink, as shown in (b) and (e). Nesting vectors are indicated by blue arrows in (f).

and VTe$_2$ as examples, we explore the origin of their CDW orders through a comprehensive *ab initio* theoretical study. This study is vital because it has been difficult to reconcile FSN and EPC so far. The main contributions of this work include an accurate description of the **q**-EPC in the whole BZ for the first time, correctly calculating the generalized static electronic susceptibility, an understanding of the CDW formation mechanism, and a comparison of the CDW gap distribution from the mean-field model with or without incorporating the EPC effects. Our results are self-consistent and emphasize the importance of EPC.

Interestingly, even in a material with a hidden one-dimensional (1D) structure in which FSN does exist [30], such as $1T$-VTe$_2$, **q**-EPC still dominates in the CDW formation. This evidence critically questions the origin of real quasi-1D CDWs. FSN has hitherto been believed to drive the CDW formation in quasi-1D materials, including NbSe$_3$ [31], (TaSe$_4$)$_2$I [32], and α-U [33], but this needs a careful investigation that includes **q**-EPC analysis. Our framework is also applicable to these materials and calls for a review of the formation mechanism of quasi-1D CDWs.

In conclusion, combining first-principles calculations and mean-field analyses, we reported a quantitative study of CDW properties in monolayer $1H$-NbSe$_2$ and $1T$-VTe$_2$. Our results confirmed the decisive role of EPC mechanism in the CDW systems. The combined analysis of FSN and EPC in both phononic and electronic pictures gives a profound understanding of the CDW formation. We argue that the same physics, in principle, should be applied to other CDW systems. The proposed analytical method can also be improved by more accurate calculations (e.g., generalized gradient approximation

$+ U$, GW, hybrid function, etc.) [29,34–36], which would allow further CDW studies in more complex systems. Our work paves a general way to unravel the physics of CDW formation with phonon and electron instabilities, which can be generalized to other CDW systems like kagome metals [37] and high-temperature superconductors [38].

APPENDIX A: THE GENERAL PROPERTIES OF MONOLAYER $1H$-NbSe$_2$ AND $1T$-VTe$_2$

The ground-state 3×3 CDW structure of monolayer $1H$-NbSe$_2$ is shown in Fig. 5(a) [14,26]. The unfolded Fermi surface and band structure of this CDW structure were used to compare our mean-field simulations in the main text [13,14,16]. Monolayer $1T$-VTe$_2$ has a Star of David in its 4×4 CDW supercell [Fig. 5(d)], in line with previous experimental results [39]. In both NbSe$_2$ and VTe$_2$, only one electronic band crosses the Fermi level [see pink bands in

Figs. 5(b) and 5(e)], which produces the Fermi surface, as shown in Figs. 5(c) and 5(f). The nesting vector in Fig. 5(f) was thought to be the origin of the anisotropic CDW gap in a previous study [18].

APPENDIX B: THE RENORMALIZED PHONON FREQUENCY

Here, we describe how electronic instability disturbs free phonon frequency. We start with free electron and phonon Green's functions:

$$G(i\omega_n, \mathbf{k}) = \frac{1}{i\omega_n - \varepsilon_{\mathbf{k}}}, \tag{B1}$$

$$D(iq_n, \mathbf{q}) = \frac{2\Omega_{\mathbf{q}}}{(iq_n)^2 - \Omega_{\mathbf{q}}^2}, \tag{B2}$$

where $\varepsilon_{\mathbf{k}}$ is the electron band energy and $\Omega_{\mathbf{q}}$ is the bare phonon frequency. Since only one electronic band crosses the Fermi level and one LA phonon branch softens to an imaginary value, the indexes of modes will be dropped hereafter. The action of an electron-phonon coupled system reads

$$S_{\text{tot}} = S_e[\bar{\psi}, \psi] + S_{\text{ph}}[\phi] + S_{\text{epc}}[\phi, \bar{\psi}, \psi], \tag{B3a}$$

$$S_e[\bar{\psi}, \psi] = -\sum_k \bar{\psi}(\omega_n, \mathbf{k})G(i\omega_n, \mathbf{k})^{-1}\psi(\omega_n, \mathbf{k}), \tag{B3b}$$

$$S_{\text{ph}}[\phi] = -\frac{1}{2}\sum_q \phi^*(q_n, \mathbf{q})D(iq_n, \mathbf{q})^{-1}\phi(q_n, \mathbf{q}), \tag{B3c}$$

$$S_{\text{epc}}[\phi, \bar{\psi}, \psi] = \sum_{k,q} g_{\mathbf{k},\mathbf{k}+\mathbf{q}}\phi(q_n, \mathbf{q})\bar{\psi}$$
$$\times (\omega_n + q_n, \mathbf{k} + \mathbf{q})\psi(\omega_n, \mathbf{k}). \tag{B3d}$$

The effective action of the phonon fields can be obtained through a random phase approximation, which reads

$$S_{\text{eff}}[\phi^*, \phi] = \frac{1}{2}\sum_q \phi(q_n, \mathbf{q})^* [-D(q_n, \mathbf{q})^{-1}$$
$$+ \sum_k |g_{\mathbf{k},\mathbf{k}+\mathbf{q}}|^2 G(i\omega_n + iq_n, \mathbf{k} + \mathbf{q})$$
$$\times G(i\omega_n, \mathbf{k})]\phi(q_n, \mathbf{q}). \tag{B4}$$

After performing the Matsubara summation, one can obtain

$$\chi(iq_n, \mathbf{q}) = \sum_{\mathbf{k}} |g_{\mathbf{k},\mathbf{k}+\mathbf{q}}|^2 \frac{f(\varepsilon_{\mathbf{k}}) - f(\varepsilon_{\mathbf{k}+\mathbf{q}})}{\varepsilon_{\mathbf{k}+\mathbf{q}} - \varepsilon_{\mathbf{k}} - iq_n}. \tag{B5}$$

Its static limit can be obtained by tuning $iq_n \to 0$; then we have the generalized static electronic susceptibility:

$$\chi_{\mathbf{q}} = \sum_{\mathbf{k}} |g_{\mathbf{k},\mathbf{k}+\mathbf{q}}|^2 \frac{f(\varepsilon_{\mathbf{k}}) - f(\varepsilon_{\mathbf{k}+\mathbf{q}})}{\varepsilon_{\mathbf{k}+\mathbf{q}} - \varepsilon_{\mathbf{k}}}. \tag{B6}$$
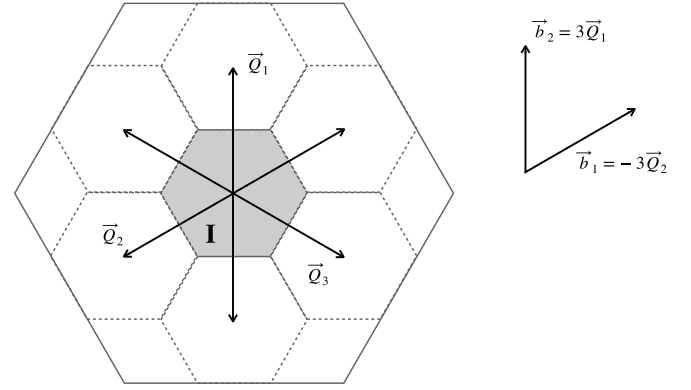
FIG. 6. The first BZ of the normal NbSe$_2$ is indicated by the black solid hexagon, the reduced BZ of the 3×3 CDW supercell is indicated by shaded region I. The CDW wave vectors are also displayed in the first BZ.

Inserting Eqs. (B2) and (B5) into Eq. (B4) gives

$$S_{\text{eff}}[\phi] = -\frac{1}{2}\sum_q \phi(q)^* \frac{(i\omega_n)^2 - \Omega_{\mathbf{q}}^2 - 2\Omega_{\mathbf{q}}\chi_{\mathbf{q}}}{2\Omega_{\mathbf{q}}}\phi(q). \tag{B7}$$

Therefore, the random phase approximation "renormalized" phonon frequency is

$$\omega_{\mathbf{q}}^2 = \Omega_{\mathbf{q}}^2 - 2\Omega_{\mathbf{q}}\chi_{\mathbf{q}}. \tag{B8}$$

APPENDIX C: MEAN-FIELD CALCULATION OF THE SPECTRAL FUNCTION

In this Appendix, we discuss the calculation for the spectral function based on a mean-field treatment of the CDW order. The mean-field Hamiltonian for the CDW phase reads

$$H_{\text{mf}} = \sum_{\mathbf{k}} \varepsilon_{\mathbf{k}} c_{\mathbf{k}}^\dagger c_{\mathbf{k}} + \sum_{\mathbf{k},\mathbf{Q}} 2g_{\mathbf{k},\mathbf{k}+\mathbf{Q}}\Delta_{\mathbf{Q}}c_{\mathbf{k}}^\dagger c_{\mathbf{k}+\mathbf{Q}} + \text{H.c.}, \tag{C1}$$

where $c_{\mathbf{k}}^\dagger$ ($c_{\mathbf{k}}$) is the electron creation (annihilation) operator and $\varepsilon_{\mathbf{k}}$ is the electron energy. For the cases in which we are interested, it is reasonable to set all $\Delta_{\mathbf{Q}}$ to be the same, i.e., $\Delta_{\mathbf{Q}} = \Delta$. For commensurate CDW order, it is better to do the summation of $\mathbf{k}$ points within the reduced BZ.

Here, we present the details for the case of NbSe$_2$. In this case, the CDW phase has a 3×3 supercell, so the reduced BZ is 9 times smaller than the original one, as shown in Fig. 6. For each $\mathbf{k}$ point in the reduced BZ, there will be another eight $\mathbf{k}$ points distributed separately within the other eight small hexagons in the original BZ. Each of these $\mathbf{k}$ points is connected to six other $\mathbf{k}$ points within this set through the CDW wave vectors.

The mean-field Hamiltonian can be written as

$$H_{\text{mf}} = \sum_{\mathbf{k}\in\mathbf{I}} \Psi_{\mathbf{k}}^\dagger h_{\mathbf{k}}\Psi_{\mathbf{k}}, \tag{C2}$$

with $\Psi_{\mathbf{k}}^{\dagger} = (c_{\mathbf{k}}^{\dagger}, c_{\mathbf{k}+\mathbf{Q}_1}^{\dagger}, c_{\mathbf{k}-\mathbf{Q}_1}^{\dagger}, c_{\mathbf{k}+\mathbf{Q}_2}^{\dagger}, c_{\mathbf{k}-\mathbf{Q}_2}^{\dagger}, c_{\mathbf{k}+\mathbf{Q}_3}^{\dagger}, c_{\mathbf{k}-\mathbf{Q}_3}^{\dagger}, c_{\mathbf{k}+\mathbf{Q}_3-\mathbf{Q}_2}^{\dagger}, c_{\mathbf{k}-\mathbf{Q}_3+\mathbf{Q}_2}^{\dagger})$ and

$$
h_{\mathbf{k}} = \begin{pmatrix}
\varepsilon_{\mathbf{k}} & \tilde{g}_{\mathbf{k},\mathbf{k}+\mathbf{Q}_1} & \tilde{g}_{\mathbf{k},\mathbf{k}-\mathbf{Q}_1} & \tilde{g}_{\mathbf{k},\mathbf{k}+\mathbf{Q}_2} & \tilde{g}_{\mathbf{k},\mathbf{k}-\mathbf{Q}_2} & \tilde{g}_{\mathbf{k},\mathbf{k}+\mathbf{Q}_3} & \tilde{g}_{\mathbf{k},\mathbf{k}-\mathbf{Q}_3} & 0 & 0 \\
\tilde{g}_{\mathbf{k}-\mathbf{Q}_1,\mathbf{k}} & \varepsilon_{\mathbf{k}+\mathbf{Q}_1} & \tilde{g}_{\mathbf{k}+\mathbf{Q}_1,\mathbf{k}-\mathbf{Q}_1} & 0 & \tilde{g}_{\mathbf{k}+\mathbf{Q}_1,\mathbf{k}-\mathbf{Q}_2} & 0 & \tilde{g}_{\mathbf{k}+\mathbf{Q}_1,\mathbf{k}-\mathbf{Q}_3} & \tilde{g}_{\mathbf{k}+\mathbf{Q}_1,\mathbf{k}+\mathbf{Q}_3-\mathbf{Q}_2} & \tilde{g}_{\mathbf{k}+\mathbf{Q}_1,\mathbf{k}-\mathbf{Q}_3+\mathbf{Q}_2} \\
\tilde{g}_{\mathbf{k}-\mathbf{Q}_1,\mathbf{k}} & \tilde{g}_{\mathbf{k}-\mathbf{Q}_1,\mathbf{k}+\mathbf{Q}_1} & \varepsilon_{\mathbf{k}-\mathbf{Q}_1} & \tilde{g}_{\mathbf{k}-\mathbf{Q}_1,\mathbf{k}+\mathbf{Q}_2} & 0 & \tilde{g}_{\mathbf{k}-\mathbf{Q}_1,\mathbf{k}+\mathbf{Q}_3} & 0 & \tilde{g}_{\mathbf{k}-\mathbf{Q}_1,\mathbf{k}+\mathbf{Q}_3-\mathbf{Q}_2} & \tilde{g}_{\mathbf{k}-\mathbf{Q}_1,\mathbf{k}-\mathbf{Q}_3+\mathbf{Q}_2} \\
\tilde{g}_{\mathbf{k}+\mathbf{Q}_2,\mathbf{k}} & 0 & \tilde{g}_{\mathbf{k}+\mathbf{Q}_2,\mathbf{k}-\mathbf{Q}_1} & \varepsilon_{\mathbf{k}+\mathbf{Q}_2} & \tilde{g}_{\mathbf{k}+\mathbf{Q}_2,\mathbf{k}-\mathbf{Q}_2} & 0 & \tilde{g}_{\mathbf{k}+\mathbf{Q}_2,\mathbf{k}-\mathbf{Q}_3} & \tilde{g}_{\mathbf{k}+\mathbf{Q}_2,\mathbf{k}+\mathbf{Q}_3-\mathbf{Q}_2} & \tilde{g}_{\mathbf{k}+\mathbf{Q}_2,\mathbf{k}-\mathbf{Q}_3+\mathbf{Q}_2} \\
\tilde{g}_{\mathbf{k}-\mathbf{Q}_2,\mathbf{k}} & \tilde{g}_{\mathbf{k}-\mathbf{Q}_2,\mathbf{k}+\mathbf{Q}_1} & 0 & \tilde{g}_{\mathbf{k}-\mathbf{Q}_2,\mathbf{k}+\mathbf{Q}_2} & \varepsilon_{\mathbf{k}-\mathbf{Q}_2} & \tilde{g}_{\mathbf{k}-\mathbf{Q}_2,\mathbf{k}+\mathbf{Q}_3} & 0 & \tilde{g}_{\mathbf{k}-\mathbf{Q}_2,\mathbf{k}+\mathbf{Q}_3-\mathbf{Q}_2} & \tilde{g}_{\mathbf{k}-\mathbf{Q}_2,\mathbf{k}-\mathbf{Q}_3+\mathbf{Q}_2} \\
\tilde{g}_{\mathbf{k}+\mathbf{Q}_3,\mathbf{k}} & 0 & \tilde{g}_{\mathbf{k}+\mathbf{Q}_3,\mathbf{k}-\mathbf{Q}_1} & 0 & \tilde{g}_{\mathbf{k}+\mathbf{Q}_3,\mathbf{k}-\mathbf{Q}_2} & \varepsilon_{\mathbf{k}+\mathbf{Q}_3} & \tilde{g}_{\mathbf{k}+\mathbf{Q}_3,\mathbf{k}-\mathbf{Q}_3} & \tilde{g}_{\mathbf{k}+\mathbf{Q}_3,\mathbf{k}+\mathbf{Q}_3-\mathbf{Q}_2} & \tilde{g}_{\mathbf{k}+\mathbf{Q}_3,\mathbf{k}-\mathbf{Q}_3+\mathbf{Q}_2} \\
\tilde{g}_{\mathbf{k}-\mathbf{Q}_3,\mathbf{k}} & \tilde{g}_{\mathbf{k}-\mathbf{Q}_3,\mathbf{k}+\mathbf{Q}_1} & 0 & \tilde{g}_{\mathbf{k}-\mathbf{Q}_3,\mathbf{k}+\mathbf{Q}_2} & 0 & \tilde{g}_{\mathbf{k}-\mathbf{Q}_3,\mathbf{k}+\mathbf{Q}_3} & \varepsilon_{\mathbf{k}-\mathbf{Q}_3} & \tilde{g}_{\mathbf{k}-\mathbf{Q}_3,\mathbf{k}+\mathbf{Q}_3-\mathbf{Q}_2} & \tilde{g}_{\mathbf{k}-\mathbf{Q}_3,\mathbf{k}-\mathbf{Q}_3+\mathbf{Q}_2} \\
0 & \tilde{g}_{\mathbf{k}+\mathbf{Q}_3-\mathbf{Q}_2,\mathbf{k}+\mathbf{Q}_1} & \tilde{g}_{\mathbf{k}+\mathbf{Q}_3-\mathbf{Q}_2,\mathbf{k}-\mathbf{Q}_1} & \tilde{g}_{\mathbf{k}+\mathbf{Q}_3-\mathbf{Q}_2,\mathbf{k}+\mathbf{Q}_2} & \tilde{g}_{\mathbf{k}+\mathbf{Q}_3-\mathbf{Q}_2,\mathbf{k}-\mathbf{Q}_2} & \tilde{g}_{\mathbf{k}+\mathbf{Q}_3-\mathbf{Q}_2,\mathbf{k}+\mathbf{Q}_3} & \tilde{g}_{\mathbf{k}+\mathbf{Q}_3-\mathbf{Q}_2,\mathbf{k}-\mathbf{Q}_3} & \varepsilon_{\mathbf{k}+\mathbf{Q}_3-\mathbf{Q}_2} & 0 \\
0 & \tilde{g}_{\mathbf{k}-\mathbf{Q}_3+\mathbf{Q}_2,\mathbf{k}+\mathbf{Q}_1} & \tilde{g}_{\mathbf{k}-\mathbf{Q}_3+\mathbf{Q}_2,\mathbf{k}-\mathbf{Q}_1} & \tilde{g}_{\mathbf{k}-\mathbf{Q}_3+\mathbf{Q}_2,\mathbf{k}+\mathbf{Q}_2} & \tilde{g}_{\mathbf{k}-\mathbf{Q}_3+\mathbf{Q}_2,\mathbf{k}-\mathbf{Q}_2} & \tilde{g}_{\mathbf{k}-\mathbf{Q}_3+\mathbf{Q}_2,\mathbf{k}+\mathbf{Q}_3} & \tilde{g}_{\mathbf{k}-\mathbf{Q}_3+\mathbf{Q}_2,\mathbf{k}-\mathbf{Q}_3} & 0 & \varepsilon_{\mathbf{k}-\mathbf{Q}_3+\mathbf{Q}_2}
\end{pmatrix}.
\tag{C3}
$$

Here, to save space, we have defined $\tilde{g}_{\mathbf{k},\mathbf{k}+\mathbf{Q}} = 2\Delta g_{\mathbf{k},\mathbf{k}+\mathbf{Q}}$. The retarded Green's function reads

$$
G_R(\omega) = (\omega + i\eta - H_{\mathrm{mf}})^{-1}.
\tag{C4}
$$

The spectral function can then be obtained accordingly. With anisotropic g, the calculated spectral function includes both FSN and EPC effects. On the other hand, with constant $|g|$ (i.e., $|g| = \sum_{\mathbf{k},\mathbf{k}+\mathbf{Q}} |g_{\mathbf{k},\mathbf{k}+\mathbf{Q}}|/N_{\mathbf{k},\mathbf{k}+\mathbf{Q}}$, where $N_{\mathbf{k},\mathbf{k}+\mathbf{Q}}$ is the number of g in the first BZ), it is a pure FSN picture. As for the case of VTe$_2$, one can perform the calculation in the same way.

APPENDIX D: FERMI SURFACE NESTING AND ELECTRON-PHONON COUPLING

Before we study the more complex generalized static electronic susceptibility $\chi_{\mathbf{q}}$ in the materials, the separate properties, FSN and EPC, should be identified.

The FSN leads to a divergence in the static Lindhard susceptibility $\chi_{\mathbf{q}}'$ at the nesting vector, which is carried over to the nesting function $\chi_{\mathbf{q}}''$:

$$
\chi_{\mathbf{q}}' = \sum_{\mathbf{k}} \frac{f(\varepsilon_{\mathbf{k}}) - f(\varepsilon_{\mathbf{k}+\mathbf{q}})}{\varepsilon_{\mathbf{k}+\mathbf{q}} - \varepsilon_{\mathbf{k}}},
\tag{D1}
$$

$$
\chi_{\mathbf{q}}'' = \sum_{\mathbf{k}} \delta(\varepsilon_{\mathbf{k}})\delta(\varepsilon_{\mathbf{k}+\mathbf{q}}),
\tag{D2}
$$

where $f(\varepsilon)$ is the Fermi-Dirac function at energy ε and δ is the delta function. The peak in $\chi_{\mathbf{q}}'$ indicates the instability of the electronic system, while $\chi_{\mathbf{q}}''$ is a direct measurement of the Fermi surface topology [4,15,40]. Generally, $\chi_{\mathbf{q}}'$ and $\chi_{\mathbf{q}}''$ produce similar fluctuations, but one should note that although we use a small value to broaden the δ function due to the finite $\mathbf{k}$ points, only $\chi_{\mathbf{q}}'$ can really capture electronic information above and below the Fermi surface (hidden nesting) [4,33,41].

As discussed in the main text, there are two theoretical methods to obtain the EPC matrix elements. The matrix element g obtained by DFPT is [29]

$$
g_{\mathbf{k},\mathbf{k}+\mathbf{q}} = \left(\frac{\hbar}{2M\omega_{\mathbf{q}}}\right)^{1/2} \langle \varphi_{\mathbf{k}+\mathbf{q}}| \partial_{\mathbf{q}}V |\varphi_{\mathbf{k}}\rangle,
\tag{D3}
$$

where $\partial_{\mathbf{q}}V$ is the derivative of the electron-ion potential, $\omega_{\mathbf{q}}$ is the phonon frequency, and $\varphi_{\mathbf{k}}$ is the electronic wave function with wave vector $\mathbf{k}$.

The EPC matrix element g obtained by the TB model is [9–12]

$$
g_{\mathbf{k},\mathbf{k}+\mathbf{q}} \propto (\nu_{\mathbf{k}} - \nu_{\mathbf{k}+\mathbf{q}})\frac{\mathbf{q}}{|\mathbf{q}|},
\tag{D4}
$$

where $\nu_{\mathbf{k}}$ is the $\mathbf{k}$ point band velocity and $\frac{\mathbf{q}}{|\mathbf{q}|}$ is the longitudinal projection, as we are interested in the LA phonon modes.

In both methods, the $\mathbf{q}$-EPC can be given by

$$
\bar{g}_{\mathbf{q}} = \sum_{\mathbf{k}} |g_{\mathbf{k},\mathbf{k}+\mathbf{q}}|^2,
\tag{D5}
$$

which is Eq. (4) in the main text. To distinguish the two different sources of EPC matrix elements, the results obtained with the TB method are labeled by superscripts ($\bar{g}_{\mathbf{q}}^{\mathrm{TB}}$ and $\chi_{\mathbf{q}}^{\mathrm{TB}}$).

In NbSe$_2$, both $\chi_{\mathbf{q}}'$ and $\chi_{\mathbf{q}}''$ [see Fig. 2(a), the blue line in Fig. 3(a), and Fig. 7(a)] have a broad plateau from $2/5\Gamma M$ to $4/5\Gamma M$, which indicates the lack of FSN. The maximum of $\bar{g}_{\mathbf{q}}^{\mathrm{TB}}$ is in the ΓK path, and its peak along ΓM is at $1/2\Gamma M$ [see Fig. 7(b) and the green line in Fig. 3(a)]. In addition, the distribution of $\chi_{\mathbf{q}}^{\mathrm{TB}}$ [Fig. 7(c)] fails to capture the phonon softening [Fig. 2(d)]. Similar analyses have been done for VTe$_2$; the peaks of $\chi_{\mathbf{q}}'$ and $\chi_{\mathbf{q}}''$ [see Fig. 2(e), the blue line in Fig. 3(c), and Fig. 7(d)] are around $2/5\Gamma M$, deviating from the CDW vector ($1/2\Gamma M$). As shown in Fig. 7(f), $\chi_{\mathbf{q}}^{\mathrm{TB}}$ derived from the TB method also does not account for the phonon softening of VTe$_2$ [Fig. 2(h)]. According to our results, compared to that from the TB method, the $\mathbf{q}$-EPC $\bar{g}_{\mathbf{q}}$ derived from DFPT is demonstrably superior. Therefore, the $\mathbf{q}$-EPC is used to explain the CDW formation in monolayer NbSe$_2$ and VTe$_2$.

APPENDIX E: SCATTERED ELECTRONS IN THE MATERIAL

$\chi_{\mathbf{q}}'$ and $\chi_{\mathbf{q}}''$ involve the sum over $\mathbf{k}$ [Eqs. (D1) and (D2)], leaving $\mathbf{q}$ as the independent variable, making them a quantitative indicator of how much Fermi surface will overlap with different translational $\mathbf{q}$. If we change the sum from over $\mathbf{k}$ to over $\mathbf{q}$, then we have

$$
\chi_{\mathbf{k}}' = \sum_{\mathbf{q}} \frac{f(\varepsilon_{\mathbf{k}}) - f(\varepsilon_{\mathbf{k}+\mathbf{q}})}{\varepsilon_{\mathbf{k}+\mathbf{q}} - \varepsilon_{\mathbf{k}}},
\tag{E1}
$$

$$
\chi_{\mathbf{k}}'' = \sum_{\mathbf{q}} \delta(\varepsilon_{\mathbf{k}})\delta(\varepsilon_{\mathbf{k}+\mathbf{q}}),
\tag{E2}
$$

which represent the elastic scattered electrons (i.e., contribute to $\chi_{\mathbf{q}}'$ and $\chi_{\mathbf{q}}''$) in the BZ. In fact, the sum of $\mathbf{q}$ normalized the outgoing electronic momenta, making $\chi_{\mathbf{k}}'$ and $\chi_{\mathbf{k}}''$ reflect only the incoming electronic momenta. Therefore, $\chi_{\mathbf{k}}'$ and $\chi_{\mathbf{k}}''$ will diverge when the incoming electronic states are close to the Fermi surface, and their colors indicate the relative contribution to $\chi_{\mathbf{q}}'$ and $\chi_{\mathbf{q}}''$ in the whole BZ. Note that the real contour of $\chi_{\mathbf{k}}''$ should be exactly the same as the Fermi surface [Figs. 8(b) and 8(d)]; its dispersed intensity is due to the
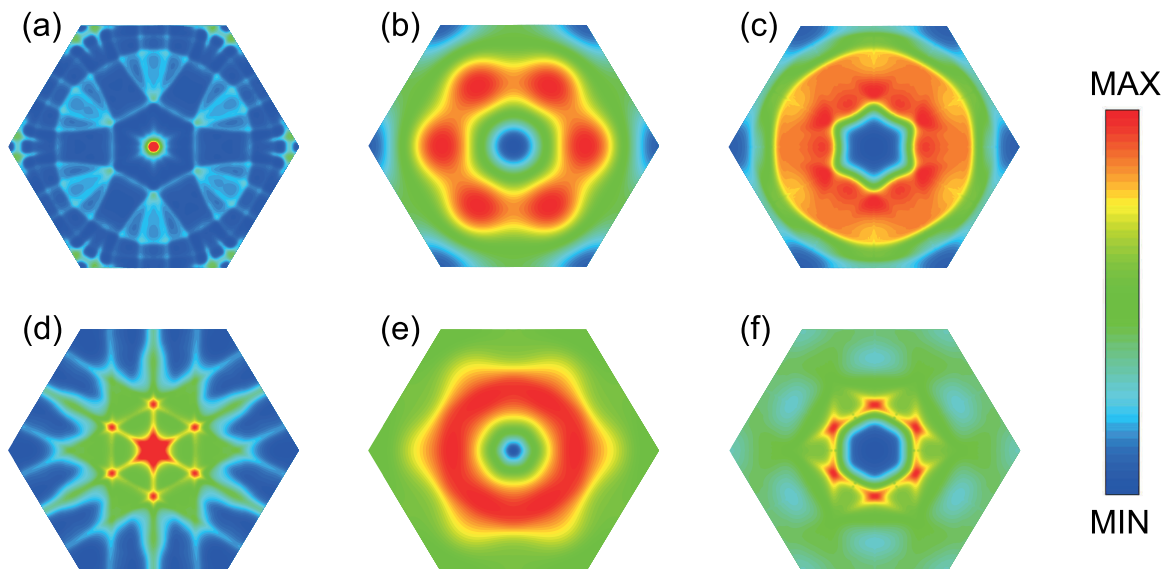
FIG. 7. (a) The nesting function $\chi''_{\mathbf{q}}$, (b) **q**-EPC $\bar{g}^{\mathrm{TB}}_{\mathbf{q}}$, and (c) generalized static electronic susceptibility $\chi^{\mathrm{TB}}_{\mathbf{q}}$ for NbSe$_2$. (d)–(f) Same as (a)–(c) but for VTe$_2$.

slight broadening used in the δ function. On the other hand, the broad range of the "hot area" in $\chi'_{\mathbf{k}}$ can be regarded as a "hidden Fermi surface" [Figs. 8(a) and 8(c)], which explains why more states are observed in $\chi'_{\mathbf{q}}$ [33].

However, the FSN picture requires the same **q** to drive a divergent peak in $\chi'_{\mathbf{q}}$, the origin of which from **k** points is thought to be the electronic gap positions. Thus, hereafter, we consider paired electrons with constrained transfer momentum $\mathbf{Q_c}$,

$$\chi'^{c}_{\mathbf{k}} = \sum_{\mathbf{q}=\mathbf{Q_c}} \frac{f(\varepsilon_{\mathbf{k}}) - f(\varepsilon_{\mathbf{k}+\mathbf{q}})}{\varepsilon_{\mathbf{k}+\mathbf{q}} - \varepsilon_{\mathbf{k}}}, \tag{E3}$$

$$\chi''^{c}_{\mathbf{k}} = \sum_{\mathbf{q}=\mathbf{Q_c}} \delta(\varepsilon_{\mathbf{k}})\delta(\varepsilon_{\mathbf{k}+\mathbf{q}}). \tag{E4}$$
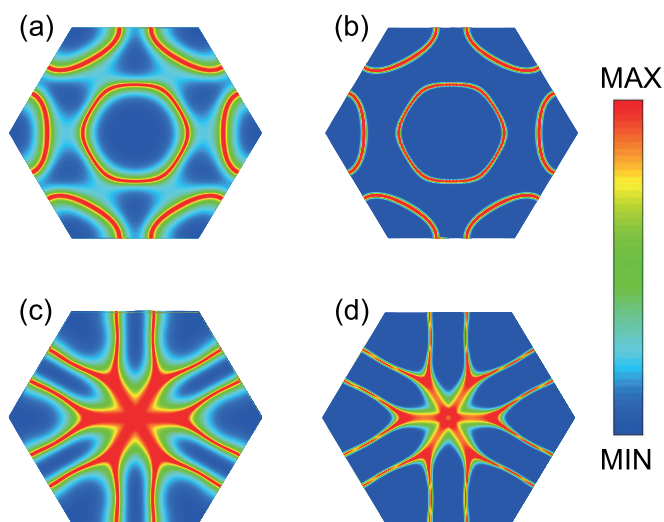
FIG. 8. (a) $\chi'_{\mathbf{k}}$ and (b) $\chi''_{\mathbf{k}}$ for NbSe$_2$; (c) $\chi'_{\mathbf{k}}$ and (d) $\chi''_{\mathbf{k}}$ for VTe$_2$.

For a better understanding of the underlying physics, the scattering processes have been disassembled according to the C_3 rotation symmetry. First, the momentum transfer **q** is considered along with the vertical direction [Figs. 9, 10(a), 10(b), 10(e), 10(f), 10(i), and 10(j)]; then their two symmetric counterparts are added to produce the point where the elastic scattering is strong (the most heavily nested point).

In NbSe$_2$, both $\chi'^{c}_{\mathbf{k}}$ and $\chi''^{c}_{\mathbf{k}}$ show peaks at the individual points [Figs. 10(a) and 10(b)], corresponding to the inter-sectant sites of the Fermi surfaces [see Fermi surfaces in Fig. 9(a)]. And $\chi'^{c}_{\mathbf{k}}$ displays more details matching the three Fermi surface pattern because of the hidden Fermi surface [Fig. 9(a)].

Figures 10(c) and 10(d) present the accumulation of Figs. 10(a) and 10(b) with their symmetric counterparts. Obviously, there is no way to argue FSN in NbSe$_2$, as "nesting" exists only at separate points. The peak of $\chi'^{c}_{\mathbf{k}}$ ($\chi''^{c}_{\mathbf{k}}$) is in the K sheet and on both sides of the ΓK path [see the red points in white circles in Figs. 10(c) and 10(d)], in line with the FSN scenario under the mean-field theory [Fig. 4(a)]. This result reflects that the opening of the CDW gap cannot be from pure FSN in NbSe$_2$.

However, in VTe$_2$, considering its CDW vector $(1/2\Gamma M)$ is inconsistent with its nesting vector $(2/5\Gamma M)$, similar analyses have been done separately. Generally, it has been argued that the long sides of the triangular pockets in VTe$_2$ will supply a strong nesting condition [18,19]. However, as revealed by the bare electronic susceptibility [see Fig. 2(e), the blue line in Fig. 3(c), and Fig. 7(d)], the VTe$_2$ Fermi surface nests at $2/5\Gamma M$ instead of $1/2\Gamma M$. Interestingly, diagnostic analyses indicate that the main contribution to $\chi'^{c}_{\mathbf{k}}$ ($\chi''^{c}_{\mathbf{k}}$) is from the K pocket edges parallel to the CDW vectors [see vertical intense spectra in Figs. 10(e), 10(f), 10(i), and 10(j)]. After considering the rotation symmetry of the nesting, it is noteworthy that when $\mathbf{Q_c} = 1/2\Gamma M$, the heavily nested points are near the apex of the triangular K pocket but not on the Fermi surface [see white circles in Figs. 10(g) and 10(h)].
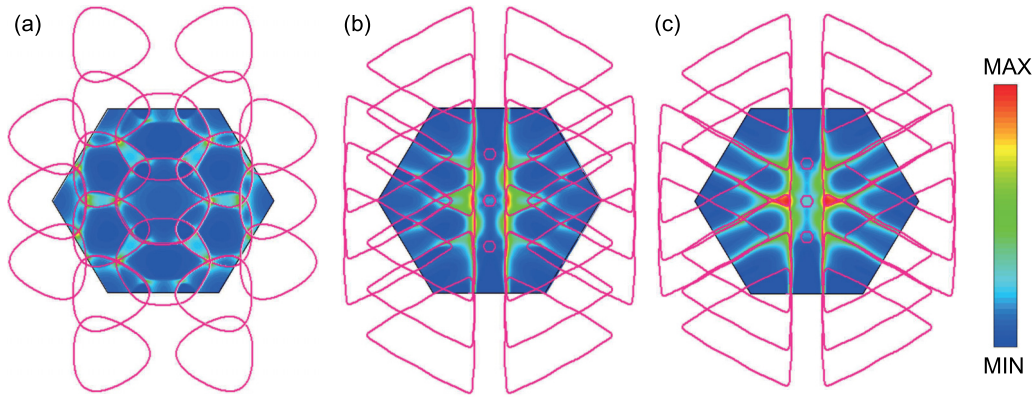
FIG. 9. The pink Fermi surfaces are moved up and down along the vertical direction of (a) NbSe$_2$ with $2/3\Gamma M$, (b) VTe$_2$ with $1/2\Gamma M$, and (c) VTe$_2$ with $2/5\Gamma M$, respectively. The calculated $\chi_{\mathbf{k}}^{\prime c}$ with $\mathbf{Q_c}$ along the vertical direction is indicated in the first BZ.

This is because not only the hidden nesting included in the static Lindhard susceptibility and small broadening used in the nesting function [33] but also the band energies are very close to the Fermi energy at the corresponding points. The dots at triangular pockets have similar spectral intensities, which is consistent with the similar spectral weights on the Fermi surface obtained with our mean-filed simulation [Fig. 4(e)]. Even if we set $\mathbf{Q_c} = 2/5\Gamma M$, the heavily nested points locate at the analogous positions. Therefore, imperfect nesting being the origin of the anisotropic gap opening in VTe$_2$ can be ruled out.
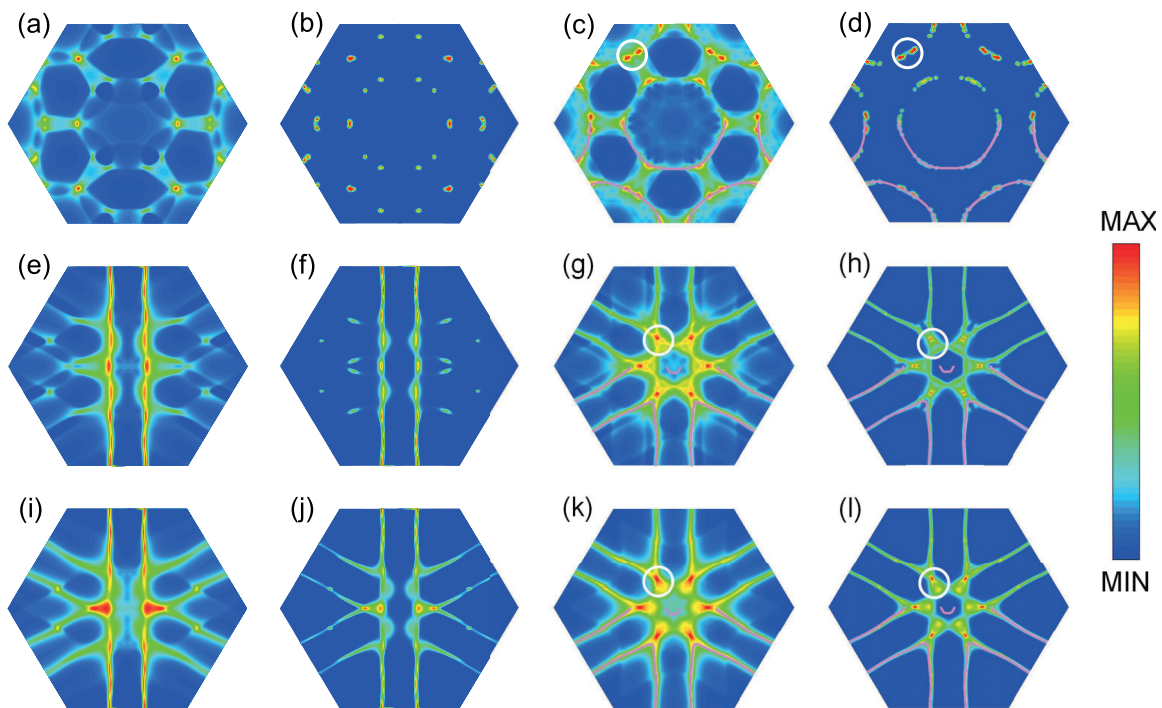
FIG. 10. The bare electronic susceptibility with constrained transfer momentum in the k space. (a) $\chi_{\mathbf{k}}^{\prime c}$ and (b) $\chi_{\mathbf{k}}^{\prime\prime c}$ for NbSe$_2$ with $\mathbf{Q_c} = 2/3\Gamma M$ along the vertical direction; (c) and (d) are the accumulation of (a) and (b) with their symmetric counterparts, respectively. (e)–(h) Same as (a)–(d), but for VTe$_2$ with $\mathbf{Q_c} = 1/2\Gamma M$. (i)–(l) Same as panels (a)–(d), but for VTe$_2$ with $\mathbf{Q_c} = 2/5\Gamma M$. In (c), (d), (g), (h), (k), and (l), the white circles indicate the most heavily nested points; the pink solid lines in the lower half of the BZ are the corresponding non-CDW Fermi surfaces.

[1] G. Grüner, The dynamics of charge-density waves, Rev. Mod. Phys. **60**, 1129 (1988).

[2] K. Rossnagel, On the origin of charge-density waves in select layered transition-metal dichalcogenides, J. Phys.: Condens. Matter **23**, 213001 (2011).

[3] X. Zhu, J. Guo, J. Zhang, and E. Plummer, Misconceptions associated with the origin of charge density waves, Adv. Phys.: X **2**, 622 (2017).

[4] M. D. Johannes and I. I. Mazin, Fermi surface nesting and the origin of charge density waves in metals, Phys. Rev. B **77**, 165135 (2008).

[5] F. Weber, S. Rosenkranz, J.-P. Castellan, R. Osborn, R. Hott, R. Heid, K.-P. Bohnen, T. Egami, A. H. Said, and D. Reznik, Extended Phonon Collapse and the Origin of the Charge-Density Wave in 2H-NbSe$_2$, Phys. Rev. Lett. **107**, 107403 (2011).

[6] X. Zhu, Y. Cao, J. Zhang, E. Plummer, and J. Guo, Classification of charge density waves based on their nature, Proc. Natl. Acad. Sci. USA **112**, 2367 (2015).

[7] R. E. Peierls, *Quantum Theory of Solids* (Oxford University Press, Oxford, 1955).

[8] W. Kohn, Image of the Fermi Surface in the Vibration Spectrum of a Metal, Phys. Rev. Lett. **2**, 393 (1959).

[9] C. M. Varma, E. I. Blount, P. Vashishta, and W. Weber, Electron-phonon interactions in transition metals, Phys. Rev. B **19**, 6130 (1979).

[10] F. Flicker and J. Van Wezel, Charge order from orbital-dependent coupling evidenced by NbSe$_2$, Nat. Commun. **6**, 7034 (2015).

[11] F. Flicker and J. van Wezel, Charge order in NbSe$_2$, Phys. Rev. B **94**, 235135 (2016).

[12] J. Henke, F. Flicker, J. Laverock, and J. Van Wezel, Charge order from structured coupling in VSe$_2$, SciPost Phys. **9**, 056 (2020).

[13] F. Zheng, Z. Zhou, X. Liu, and J. Feng, First-principles study of charge and magnetic ordering in monolayer NbSe$_2$, Phys. Rev. B **97**, 081101(R) (2018).

[14] C.-S. Lian, C. Si, and W. Duan, Unveiling charge-density wave, superconductivity, and their competitive nature in two-dimensional NbSe$_2$, Nano Lett. **18**, 2924 (2018).

[15] P. Chen, W. W. Pai, Y.-H. Chan, V. Madhavan, M.-Y. Chou, S.-K. Mo, A.-V. Fedorov, and T.-C. Chiang, Unique Gap Structure and Symmetry of the Charge Density Wave in Single-Layer VSe$_2$, Phys. Rev. Lett. **121**, 196402 (2018).

[16] F. Zheng and J. Feng, Electron-phonon coupling and the coexistence of superconductivity and charge-density wave in monolayer NbSe$_2$, Phys. Rev. B **99**, 161119(R) (2019).

[17] M. Calandra, I. I. Mazin, and F. Mauri, Effect of dimensionality on the charge-density wave in few-layer 2H-NbSe$_2$, Phys. Rev. B **80**, 241108(R) (2009).

[18] Y. Wang, J. Ren, J. Li, Y. Wang, H. Peng, P. Yu, W. Duan, and S. Zhou, Evidence of charge density wave with anisotropic gap in a monolayer VTe$_2$ film, Phys. Rev. B **100**, 241404(R) (2019).

[19] K. Sugawara, Y. Nakata, K. Fujii, K. Nakayama, S. Souma, T. Takahashi, and T. Sato, Monolayer VTe$_2$: Incommensurate Fermi surface nesting and suppression of charge density waves, Phys. Rev. B **99**, 241404(R) (2019).

[20] P. Giannozzi *et al.*, Quantum Espresso: A modular and open-source software project for quantum simulations of materials, J. Phys.: Condens. Matter **21**, 395502 (2009).

[21] P. Giannozzi *et al.*, Advanced capabilities for materials modelling with Quantum Espresso, J. Phys.: Condens. Matter **29**, 465901 (2017).

[22] D.R. Hamann, Optimized norm-conserving Vanderbilt pseudopotentials, Phys. Rev. B **88**, 085117 (2013).

[23] S. Poncé, E. R. Margine, C. Verdi, and F. Giustino, EPW: Electron–phonon coupling, transport and superconducting properties using maximally localized Wannier functions, Comput. Phys. Commun. **209**, 116 (2016).

[24] D. Lin, S. Li, J. Wen, H. Berger, L. Forró, H. Zhou, S. Jia, T. Taniguchi, K. Watanabe, X. Xi *et al.*, Patterns and driving forces of dimensionality-dependent charge density waves in 2H-type transition metal dichalcogenides, Nat. Commun. **11**, 2406 (2020).

[25] X. Xi, L. Zhao, Z. Wang, H. Berger, L. Forró, J. Shan, and K. F. Mak, Strongly enhanced charge-density-wave order in monolayer NbSe$_2$, Nat. Nanotechnol. **10**, 765 (2015).

[26] M. M. Ugeda, A. J. Bradley, Y. Zhang, S. Onishi, Y. Chen, W. Ruan, C. Ojeda-Aristizabal, H. Ryu, M. T. Edmonds, H.-Z. Tsai *et al.*, Characterization of collective ground states in single-layer NbSe$_2$, Nat. Phys. **12**, 92 (2016).

[27] Y. Nakata, K. Sugawara, S. Ichinokura, Y. Okada, T. Hitosugi, T. Koretsune, K. Ueno, S. Hasegawa, T. Takahashi, and T. Sato, Anisotropic band splitting in monolayer NbSe$_2$: Implications for superconductivity and charge density wave, npj 2D Mater. Appl. **2**, 12 (2018).

[28] P. M. Coelho, K. Lasek, K. Nguyen Cong, J. Li, W. Niu, W. Liu, I. I. Oleynik, and M. Batzill, Monolayer modification of VTe$_2$ and its charge density wave, J. Phys. Chem. Lett. **10**, 4987 (2019).

[29] F. Giustino, Electron-phonon interactions from first principles, Rev. Mod. Phys. **89**, 015003 (2017).

[30] M. H. Whangbo and E. Canadell, Analogies between the concepts of molecular chemistry and solid-state physics concerning structural instabilities. electronic origin of the structural modulations in layered transition metal dichalcogenides, J. Am. Chem. Soc. **114**, 9587 (1992).

[31] C. W. Nicholson, C. Berthod, M. Puppin, H. Berger, M. Wolf, M. Hoesch, and C. Monney, Dimensional Crossover in a Charge Density Wave Material Probed by Angle-Resolved Photoemission Spectroscopy, Phys. Rev. Lett. **118**, 206401 (2017).

[32] W. Shi, B. J. Wieder, H. L. Meyerheim, Y. Sun, Y. Zhang, Y. Li, L. Shen, Y. Qi, L. Yang, J. Jena *et al.*, A charge-density-wave topological semimetal, Nat. Phys. **17**, 381 (2021).

[33] A. P. Roy, N. Bajaj, R. Mittal, P. D. Babu, and D. Bansal, Quasi-One-Dimensional Fermi Surface Nesting and Hidden Nesting Enable Multiple Kohn Anomalies in α-Uranium, Phys. Rev. Lett. **126**, 096401 (2021).

[34] J.-J. Zhou, J. Park, I. Timrov, A. Floris, M. Cococcioni, N. Marzari, and M. Bernardi, *Ab Initio* Electron-Phonon Interactions in Correlated Electron Systems, Phys. Rev. Lett. **127**, 126404 (2021).

[35] Z. Li, G. Antonius, M. Wu, F. H. daJornada, and S. G. Louie, Electron-Phonon Coupling From *Ab Initio* Linear-Response Theory Within the *GW* Method: Correlation-Enhanced Interactions and Superconductivity in Ba$_{1-x}$K$_x$BiO$_3$, Phys. Rev. Lett. **122**, 186402 (2019).

[36] Z. P. Yin, A. Kutepov, and G. Kotliar, Correlation-Enhanced Electron-Phonon Coupling: Applications of *GW* and

Screened Hybrid Functional to Bismuthates, Chloronitrides, and Other High-T_c Superconductors, Phys. Rev. X **3**, 021011 (2013).

[37] H. Tan, Y. Liu, Z. Wang, and B. Yan, Charge Density Waves and Electronic Properties of Superconducting Kagome Metals, Phys. Rev. Lett. **127**, 046401 (2021).

[38] X. Wang, Y. Yuan, Q.-K. Xue, and W. Li, Charge ordering in high-temperature superconductors visualized by scanning tunneling microscopy, J. Phys.: Condens. Matter **32**, 013002 (2020).

[39] M. Liu, C. Wu, Z. Liu, Z. Wang, D.-X. Yao, and D. Zhong, Multimorphism and gap opening of charge-density-wave phases in monolayer VTe_2, Nano Res. **13**, 1733 (2020).

[40] Z. Wang, J. Zhou, K. P. Loh, and Y. P. Feng, Controllable phase transitions between multiple charge density waves in monolayer $1T\text{-}VSe_2$ via charge doping, Appl. Phys. Lett. **119**, 163101 (2021).

[41] M.-H. Whangbo, E. Canadell, P. Foury, and J.-P. Pouget, Hidden Fermi surface nesting and charge density wave instability in low-dimensional metals, Science **252**, 96 (1991).